WILEY-VCH

Title: Low-Dimensional Conduction Mechanisms in Highly-Conductive and Transparent Conjugated Polymers

Asli Ugur, Ferhat Katmis, Mingda Li, Lijun Wu, Yimei Zhu, Kripa K. Varanasi*, Karen K. Gleason*

A. Ugur, Prof. K. K. Gleason
Department of Chemical Engineering, Massachusetts Institute of Technology, Cambridge, Massachusetts 02139, USA
E-mail: kkg@mit.edu

A. Ugur, Prof. K. K. Varanasi
Department of Mechanical Engineering, Massachusetts Institute of Technology, Cambridge, Massachusetts 02139, USA
E-mail: varanasi@mit.edu

F. Katmis
Department of Physics, Massachusetts Institute of Technology, Cambridge, Massachusetts 02139, USA

M. Li
Department of Nuclear Science and Engineering, Massachusetts Institute of Technology, Cambridge, Massachusetts 02139, USA

L. Wu, Prof. Y. Zhu
Condensed Matter Physics & Materials Science Department, Brookhaven National Laboratory, Upton, NY 11973, USA

Charge transport mechanisms in conjugated polymers are widespread interest for enabling high-performance and low-cost optoelectronic and thermoelectric devices.[1] Optimal device performance for high-end technologies requires a fundamental grasp of transport properties at the nanoscale.[2] However, the understanding of conduction mechanisms remains incomplete even after several decades of intensive investigation.[3] Recently clues have emerged which shed light

on complicated microscale conduction pathways.[4] These exciting finders further the debate on charge transport in conducting polymers, which are neither fully amorphous nor completely crystalline. There is a strong tendency for collective charge motion along the ordering direction of the polymer chains where strong covalent bonds form along the same direction.[5] In addition, strong backbone, length of the conjugation chain and most importantly polymer crystallinity have important effects on conduction. Charge-carrier mobility depends not only on polymer crystallinity and crystallite orientation at nanoscale, but also on the connectivity of macroscopic domains and morphological imperfections.[5] Among the conjugated polymers, poly (3,4-ethylenedioxythiophene) (PEDOT) displays a valuable combination of high electrical conductivity and stability. PEDOT is desired for commercial applications including photodiodes, capacitors, sensors, and organic light-emitting diodes,[6] and is also a promising candidate for integration into future macro- and thermo-electronic devices.[7, 8] The desirable features of PEDOT derive from the chemical structure of the 3,4-ethylenedioxythiophene monomer.[9] The backbonded ring at 3,4-positions of the 5-member thiophene ring allows polymerization to occur only through the 2,5- positions. The resulting conjugated PEDOT chains have a linear structure and hence a propensity to crystallize. In addition, the pair of electronegative oxygen atoms in the backbonded ring stabilizes the presence of the cationic doping species required for conductivity. Previously, we have reported oxidative chemical vapor deposition (oCVD) as a means of synthesizing conductive PEDOT layers.[10] Additionally, we demonstrated the ability to graft PEDOT directly to its substrate. The covalent chemical bonds formed across the interface eliminate cracking and delamination; which facilitates well-defined lithographic patterns to resolved in PEDOT for feature size as small as 60 nm.[11]

In the current work, the oCVD synthesis of PEDOT is utilized to control crystallite size as well as the orientation of these ordered domains. Significant increases in crystallite sizes are achieved by increasing deposition temperature. Additionally, we show for the first time that oCVD grafting produce transverse alignment of polymer chains in the crystalline domains in the near interface region. These uniquely structured polymer films allows us to quantitatively access the predictions of different charge transport models. We show that, the electrical conductivity increases with increasing crystallite sizes and interestingly, with decreasing thickness in contrast to inorganic materials. For these observations a linear combination of Mott`s and Efros-Shklovskii`s variable range hopping (ES-VRH) models is used that provides an explanation for the dimensionality of the films and the inter-crystallite hopping. Based on the excellent agreement between direct experimental evidence and our model, we hypothesize that high overlap of the total wavefunctions of the ground state of the charges at each crystalline domain, which increases with increased crystal domain size; is the main reason for the increased conductivity. For ultrathin films, the conductivity can be well described by Mott`s VRH for highly ordered structures. However, the ES-VRH model, which applies to disordered systems,[12] is needed to quantitatively predict the data for thicker films. Increased disorder results in 3D conduction pathways that diminish the charge transport; in contrast, less disordered (2D) utra-thin films have lower resistances since the conduction pathways are better aligned. In the future, we anticipate the ability to differentially influence the transport of phonons and charge carriers across grafted versus ungrafted interfaces as a key means by which thermoelectric interfaces employing PEDOT can be fundamentally understood and optimized.

The grafted and ungrafted oCVD PEDOT thin films were grown on Si(100) having a native oxide layer (experimental details can be found in the supplementary online materials (SOM)).

oCVD is a one step process in which both monomer and oxidant ($FeCl_3$) are delivered in the vapor phase in a vacuum. Silicon substrates are exposed to 3,4-ethylenedioxythiophene monomer delivered from a monomer jar from a side of the vacuum chamber. The substrate temperature varied from 100 to 200 °C under ~ 0.1 mTorr chamber pressure. For all depositions the flow rate of PEDOT is kept constant at ~ 5 sccm and deposition time varying from 15 to 60 min. To graft PEDOT, a silane coupling agent is used to form a robust bonding transition from inorganic to organic material. The (100) oriented silicon substrate with native silicon oxide layer is treated with oxygen plasma (29.6 watts, 15 min) to form hydroxyl groups. The sample is then exposed to trichlorovinylsilane (TCVS – $C_2H_3SiCl_3$) to form a vinyl terminated surface to which PEDOT can graft.

X-ray diffraction (XRD) measurements were carried out using CuK$_{\alpha 1}$ radiation on both grafted and ungrafted films. Large area XRD mapping further reveals the distribution of crystallite orientations through two types of reflections, (h00) and (0k0). For the ungrafted samples (**Figure 1b**), the predominant reflection is (0k0), corresponding to the PEDOT backbone aligned parallel surface and packed together with the π-π stacking direction, which is perpendicular (**Figure 1a**(ii)) to the plane of the substrate. This orientation is known as face-on packing. In contrast, for the grafted film, both (0k0) and (h00) diffraction families are observed (**Figure 1c**). The presence of the (h00) reflection is clear evidence that grafting creates a new population of crystalline domains in which the backbone of the PEDOT chain is oriented, likewise, parallel to the surface, however, with the π-π stacking parallel to the plane of the substrate surface (**Figure 1a**(i)). This orientation is known as edge-on packing. Existence of vinyl bonds at the interface, which are created by pre-treatment of the substrate, changes the surface energy and forces to change the

bond type from weak van der Waals bonds to strong covalent bonds at the interface. These created bonds might force the backbone of the polymer to pack in a different orientation. Grafted orientation represents ~79% of all oriented domains in this 180 nm thick film, which is calculated by using Scherrer equation.[13] We hypothesize that the grafted chains are in the near interface region, since the grafting starts at the interface where viny bonds are created and that thinner films would display a higher fraction of the grafted orientation. There is also a small fraction of perpendicular orientated backbone to the substrate surface (**Figure 1a**(iii)) for grafted films, which is not observable with XRD, however these domains are visible in transmission electron microscopy images on grafted samples (see SOM **Figure S7**).

Choosing between grafted and ungrafted oCVD PEDOT offers bottom-up controllability of the polymer films, which also provides control of the electrical properties. Here the highest in-plane conductivity values are obtained for the ungrafted films (**Figure 4**) for which the XRD reveals only ($0k0$)–oriented crystallites. In these crystallites, the conjugated PEDOT backbone is aligned parallel to the substrate (**Figure 1**), where the π-π stacking is perpendicular to the substrate surface which is the densest packing configuration and hence the most efficient transport pathway. Thus, the conductivity results demonstrate that the crystallization and alignment of the PEDOT chains along the substrate on the nanoscale improve the macroscopically observed charge transport along the same direction. The orientation of a single chain determines the contribution of polarons, while the order packing of multiple aligned chains influences the contribution of the bipolarons.[8]

It is important to realize if domain boundaries have lower electrostatic potential than the crystalline domains, and the domains themselves have been hypothesized to be charge trapping centers.[14] Mean crystallite sizes dervived from the Scherrer equation[13] from the observed XRD linewidths are 3 nm for ($0k0$) and 5.5 nm for ($h00$)-type oriented crystallites. If scattering from the crystallites and their domain boundaries dominated the charge transport in the PEDOT films, we would expect the ungrafted film which is comprised entirely of the smaller ($0k0$) oriented crystals to have a reduced conductivity relative to its grafted counterpart. However the opposite is observed (**Figure 4**), suggesting that another mechanism dominates the charge transport.

To better understand the role of the nanoscale crystallinity on electrical conductivity, advanced electron microscopy measurements were undertaken to reveal the distribution of crystallite sizes present in the oCVD PEDOT films. These measurements complement the XRD results and provide direct proof of the well-controlled chain alignment. Trends in the distribution of domain sizes with variation in substrate temperature in the grafted films were found to be similar to their ungrafted counterparts. The nanocrystalline films contain highly ordered regions separated by disordered (amorphous) chains (see schematic illustration in SOM as **Figure S3**) and effects of temperature on formation of such domains are crucial. The existence of different size of domains is confirmed by the high angle annular dark field (HAADF) images with scanning transmission electron microscopy (STEM), where image contrast is roughly proportional to the square of the atomic number of probing chemical species (the HAADF images are shown in **Figure 2**). The HAADF images of the grafted PEDOT films grown at 100 °C and 200 °C substrate temperatures are shown in **Figure 2a** and **b**, respectively. The left region is the substrate and SiO_2, while the

pink region on the right is the Pt protection layer. The PEDOT thin film is sandwiched in the

middle (dark blue). In order to verify the domain distribution and sizes of the crystalline PEDOT

inside the thin film, high-resolution HAADF images are obtained (**Figure 2c** and **d**) in STEM

mode. The crystalline structures in the PEDOT are clearly seen in the magnified images **Figure**

2c and **d**.

Both the size distribution of the domains and their inter-domain spaces change with deposition

temperatures (**Figure 2e**). At low temperature, the domain sizes are small (~2 nm) as shown by a

single peak in the histogram. At elevated temperature, the scenario changes dramatically and

leads to significant increase in conductivity (**Figure 4a-b**). As seen in the **Figure 2b-d**, the

crystalline sizes dramatically increase, up to 10 nm, indicating either by direct growth of larger

domains or coalescence of small domains induced by the increased mobility of the polymer

chains at elevated temperatures. The later hypothesis is consistant with some small domains

remaining in regions between the larger domains, which are indeed observed in the histogram.

The remarkable ordering of PEDOT crystallite sites resulting from oCVD synthesis may

facilitate hopping of electrons between the crystalline domains. In order to further verify the

hopping conduction mechanism, we performed temperature-dependent electrical transport

measurements and analyzed these results using a "coarse–grained" variable range hopping

(VRH) model. The original VRH model describes the low-temperature conductivity caused by

the hopping from localized electrons[15] from one atomic site to another. In the present situation,

instead of atomic sites, intra-crystallite conduction electrons (i.e. extended electron clouds) are

considered localized when hopping among crystallites (inter-crystallite hopping). This hopping

contributes to the total electrical conductivity (**Figure 3a**). Therefore, the hopping is no longer

from one atomic site to its neighbor atoms, but "coarse-grained" from one crystallite site to

another. When the crystallites are larger, the overlap between their total wavefunctions increases,

leading to improved transport pathways in which the resistive amorphous areas no longer

dominate the overall conductivity. The Mott's VRH applies to the condition where Coulomb

interactions between the localized electrons are negligible. When inter-crystallite long-range

Coulomb interactions becomes significant, these interactions open up a soft Coulomb gap, as

described by the Efros-Shklovskii (ES) type of VRH.[16] The total normalized resistivity can be

empirically treated as a linear combination of Mott's VRH and

ES-VRH:

$$\frac{\rho(\text{T}_{eff})}{\rho(300\text{K})} = \left(\beta_1 \exp\left[-\left(T_M\ /\ T\right)^{\frac{1}{1+d}}\right] + \beta_2 \exp\left[-\left(T_{ES}/T\right)^{\frac{1}{2}}\right]\right)^{-1}, \qquad (1)$$

where β_1 and β_2 are dimensionless amplitudes for the Mott and ES type of conductivity,

respectively, and their ratio determines whether Coulomb interaction is significant or not. The

samples that are less disordered can overcome these interactions and the conduction can be

explained purely with Mott`s VRH. On the other hand, with increased disorder the ES-VRH

starts to arise. T_{M} is Mott's transition temperature for the onset of conduction, and T_{ES} is the ES

type VRH transition temperature which satisfies $T_{\text{ES}} \propto 1/\varepsilon$, where ε is the dielectric constant. In

the first term of Eq. 1, the exponent, d, is the effective dimensionality for the Mott-type

conduction which determines the dimension of the film

The "coarse-grained" VHR model (Eq. 1) provides a superb description of the observed

temperature dependence of resistivity from room temperature down to 10 K, measured using the

conventional Van der Pauw geometry (**Figure 3b**). The value at 0 K is obtained by spline

extrapolation (**Figure 3b**, inset). Semiconductor-like behavior, $d\rho/dT$, is observed for all

samples. Since the ungrafted samples display both the highest conductivies and only a single

crystal orientation, we selected only the the ungrafted for measurement of the temperature

dependent transport characteristics. A non-linear least squares regression of the observed change

in conductivity with temperature (**Figure S5** in SOM) for each of the 3 samples measured is

performed against Eq. (1) by forcing sample #1 to be 3D, sample #2 to be 2D, and sample #3 to

be 2D, as tabulated in **Tab. S3** in SOM. Sample #1, which has the lowest resistivity, is deposited

at 200 °C with conductivity of 2050 S/cm (52 nm), Sample #2 has an intermediate resistivity

which is also deposited at 200 °C but is thicker (124 nm) than sample #1 with conductivity of

885 S/cm, and Sample #3 has the highest resistivity with lower preparation temperature, 100 °C

with conductivity of 320 S/cm (145 nm). All three samples were post rinsed with 5 mol L^{-1} HBr

acid to remove the excess oxidant and dope films with Br- counter-anions to obtain low

resistivity layers. From the table we see directly when we fix the incorrect value for

dimensionality and let the nonlinear optimization runs, the residual (sum of mean square error)

increases significantly. For sample #1, the thinnest of the set, $d = 2$ (2D), in contrast, both

thicker samples, #2 and #3, $d = 3$ (3D) provides the statistically best regression to the data, as

shown in **Figure 3b** and table in **Tab. S3** in SOM. Samples #1, the thinnest among the samples,

displays good agreement with pure Mott's VRH, (e.g. $\beta_2 = 0$ in Eq. 1; see SOM for detail) where

there is no contribution of ES-VRH. However, it can be seen in **Figure S4** in SOM that the

fitting has some deviations for all samples, when only Mott`s VRH is used. Therefore, ES-VRH

is also included where the fittings become excellent as shown in **Figure 3b**. Even though sample

#1 and sample #2 are prepared with the same deposition temperature (200 °C) due to increased

disorder in the thicker films, explained by ES-VRH, the charge transport pathways become 3D,

which increases the resistivity of the films. The same effect is also observed more extensively for

sample #3 that is deposited at the lower substrate temperature of 100 °C, with comparable

thickness to sample #2. This sample has smaller crystallites as shown in **Figure 2a** compared to

the films deposited at higher temperatures in **Figure 2b**. A remarkably good match is obtained

between the resistivity data and Eq. 1 (Mott+EH VRH); for sample #2 $\beta_2 = 6.74$, and for sample

#3, $\beta_2 = 116.2$, which indicate a ~ 77.5% and 96.8% contribution of the ES-VRH conduction

model, respectively, representing significant inter-crystallite Coulomb interaction. For sample

#1, $\beta_2 = 0.69$ indicating the weakest contribution of ES-VRH (46%). In sample #3, the origin of

the weaker Coulomb screening effect is consistent with a higher fraction of amorphous regions,

since amorphous regions generally have smaller dielectric constant ε compared with crystalline

regions. It would be expected to have the lowest dielectric constant and correspondingly the

weakest Coulomb screening effect.

Moreover, since $T_M \propto (1/S)^3$ where S is the average crystallite size, values of T_M extracted from

Eq. 1 correspond to an average crystalline size ratio S1:S2:S3 ~ 3:2:1. This ratio is consistent

with the direct observation of crystallite size by HAADF, where the higher deposition

temperature leads to larger crystallite size. Obtained crystalline size ratio coincides with the

values of T_{ES} obtained from Eq. 1. Sample #3 has largest T_{ES}, together with the largest increase

of resistivity at low temperature (SOM). The room temperature conductivity for all samples

reduces while decreasing the temperature. The most obvious trends observed here is that sample

#3 shows much larger variation in resistivity near 0 K than the other two samples and that this

observation is additional support of the contribution of the ES-VRH conduction mechanism in

sample #3. To generalize a relation for 2D and 3D type samples, the reduction of resistivity as

dimension d decreases, at various sizes of domains, are generic. The logarithmic of normalized

resistivity ratio $\log(\rho_{2D}/\rho_{3D})$ $\left(\dfrac{\rho_{2D}}{\rho_{3D}} \equiv \dfrac{\rho_{2D}(\mathrm{T})/\rho_{2D}(300\,\mathrm{K})}{\rho_{3D}(\mathrm{T})/\rho_{3D}(300\,\mathrm{K})} \right)$ between a 2D and 3D-like samples are shown

in **Figure 3c**. If two samples have the same domain sizes, with identical T_{M}, the resistivity

increases more rapidly in 3D sample. The parameters are taken from 2D-like sample #1 and 3D-

like sample #3, respectively, but keeping them with the same. It can be seen directly that $\rho_{2D} < \rho_{3D}$

is valid as long as T>30 K.

It is desirable to establish the limitations for controlling the conductivity within the variety of

polymer films. For this purposes, we analyze the different parameters one-by-one hitherto for

mostly between so called 3D- and 2D-like arrays of PEDOT crystallites. To further enlarge the

hypothesis of 2D vs. 3D conduction, three sets of film thickness ranges were investigated; *i)*

ultra-thin limit, less than 10 nm, *ii)* intermediate case of between 10 nm up to 80 nm, and *iii)*

bulk-dominated phase where thicknesses are thicker than 100 nm. For films thinner than 80 nm,

we hypothesize that the surface helps drive ordered assembly of the crystallites of the first

crystallites formed. At each substrate temperature over the range (except for ultra-thin films)

from 100 to 200 °C, four variants were prepared: grafted or ungrafted films which were either

rinsed with methanol only or additionally rinsed with HBr. For the intermediate thicknesses

films, for each of the 4 variants, the conductivity (σ) increased monotonically with substrate

temperature (**Figure 4a**). The highest conductivities for the intermediate thickness range, σ ~

2000 S/cm, is achieved for the ungrafted and HBr rinsed condition at a substrate temperature of

200 °C. The next highest values, σ ~ 1800 S/cm, are observed with grafted and HBr rinsed

sample grown at the same substrate temperature. The HBr rinsed films generally have about two

times higher conductivity than their comparable MeOH only rinsed counter parts. Pairwise

comparison between the ungrafted and grafted films, which experienced the same rinsing

treatment, reveals that grafting reduces conductivity in all but one case. To further probe the

effect of thickness on conductivity, samples with less than 10 nm thicknesses were deposited at

the 150, 175 and 200 °C substrate temperatures which were ungrafted and HBr rinsed. An

increase in conductivity close to 3700 S/cm is obtained for high growth temperatures (presented

in **Figure 4a** as star symbols), which is a clear indication that these nanoscale layers have

improved charge transport properties. In **Figure 4b**, all the films measured were above 100 nm

thick. All the same trends with substrate temperature, grafting and rinsing are observed in **Figure**

4a are found again in **Figure 4b**. Notably, in the thicker films of **Figure 4b**, the conductivities

are lower than observed for their thinner counterparts shown in **Figure 4a**.

Next generation optoelectronic devices, such as displays, solar-cells or touch screens, require

flexibility and processability over large areas. Currently, Indium tin oxide (ITO) is used as

transparent electrode material extensively that has ideal optoelectronic properties. However, ITO

suffers from high cost and brittleness. These two major drawbacks hinder the use of ITO in

large-area flexible electronics for next generation devices. Transparent and conductive polymers

are promising candidates that could replace ITO with their low cost and processability. The ultra-

thin PEDOT films (<10 nm) that are studied in this work have excellent transparencies that

reached up to ~ 98% (**Figure S6** in SOM) at 550 nm with sheet resistances down to 500 $\Omega/\square$. To

analyze optical figure of merit for conducting transparent thin films, the following equation is

used where transmittance (T) and sheet resistance (R_s) are linked;

$$T = (1 + \frac{Z_0}{2R_s} \frac{\sigma_{dc}}{\sigma_{op}})$$ (2)

where Z_0 is the impedance of free space (377 Ω). The dc conductivity to optical conductivity ratio

(σ_{dc}/σ_{op}), increases with increasing deposition temperature and reaches up to ~35.3 for 200 °C for

PEDOT films (**Figure 4c**) which is comparable with the literature values for PEDOT:PSS and

sufficient for transparent electrode applications.[17]

In summary, the combination of multiple characterization methods and controlled synthesis by

oCVD gives rise to deeper understanding of the charge transport properties of PEDOT polymer

films. In ungrafted films, the PEDOT chains are primarily in face-on configuration. Crystallites

with this same orientation were observed in grafted films; however, in addition, a significant

fraction of crystallites also formed in the edge-on configuration. There is also a small fraction of

crystallites, where the backbone is aligned perpendicular to the substrate for grafted films.

However, the latter configuration is only observable with STEM. For both grafted and ungrafted

films, increasing substrate temperature had the largest impact on increasing conductivity where

the domain sizes are clearly visualized by STEM. Additionally, Br doping resulting from acid

rinsing consistently decreases the sheet resistance for both grafted and ungrafted films. We

successfully applied the coarse-grained variable range hopping theory, which describes the inter-

crystallite electron hopping, to explain the resistivity as a function of temperature. Despite the

extended electronic state within one crystallite, it is the overlap between the extended intra-

crystallite electronic states which contributes to the final conductivity. Most importantly, the

effect of dimensions (2D vs 3D) and the crystalline domain sizes were extracted from the model,

and showed excellent agreement with both X-ray and electron diffraction based results. This

paves the pathway for the new mechanism of conductivity enhancement, in addition to the

conduction within polymer chain. Electrical conduction in conjugated polymeric nanolayers is crucial to the emerging technological interest for high performance optoelectronic and thermoelectric devices.

Methods

Detailed description of sample preparation for deposition by oCVD and STEM characterization, XRD measurement configuration and details about modelling is provided in supplementary online materials (SOM).

Supporting Information

Supporting Information is available from the Wiley Online Library or from the author.

Acknowledgements

Received: ((will be filled in by the editorial staff))
Revised: ((will be filled in by the editorial staff))
Published online: ((will be filled in by the editorial staff))

[1]   J. H. Burroughes, D. D. C. Bradley, A. R. Brown, R. N. Marks, K. Mackay, R. H. Friend, P. L. Burns, A. B. Holmes, Nature 1990, 347, 539; G. Gustafsson, Y. Cao, G. M. Treacy,

F. Klavetter, N. Colaneri, A. J. Heeger, Nature 1992, 357, 477; N. S. Sariciftci, L. Smilowitz, A. J. Heeger, F. Wudl, Science 1992, 258, 1474; N. Tessler, G. J. Denton, R. H. Friend, Nature 1996, 382, 695; P. K. Ho, Science 1999, 285, 233; D. Bhattacharyya, R. Yang, K. K. Gleason, Journal of Materials Chemistry 2012, 22, 17147; R. Venkatasubramanian, E. Siivola, T. Colpitts, B. O'Quinn, Nature 2001, 413, 597; A. I. Hochbaum, R. Chen, R. D. Delgado, W. Liang, E. C. Garnett, M. Najarian, A. Majumdar, P. Yang, Nature 2008, 451, 163; B. Poudel, Q. Hao, Y. Ma, Y. Lan, A. Minnich, B. Yu, X. Yan, D. Wang, A. Muto, D. Vashaee, X. Chen, J. Liu, M. S. Dresselhaus, G. Chen, Z. Ren, Science 2008, 320, 634.

[2] T. Takano, H. Masunaga, A. Fujiwara, H. Okuzaki, T. Sasaki, Macromolecules 2012, 45, 3859; J. L. Brédas, F. Wudl, A. J. Heeger, Solid State Communications 1987, 63, 577; W. P. Su, J. R. Schrieffer, A. J. Heeger, Phys Rev Lett 1979, 42, 1698; A. J. Heeger, S. Kivelson, J. R. Schrieffer, W. P. Su, Rev Mod Phys 1988, 60, 781.

[3] Y. Cao, G. M. Treacy, P. Smith, A. J. Heeger, Applied Physics Letters 1992, 60, 2711; N. S. Sariciftci, A. J. Heeger, Y. Cao, Physical Review B 1994, 49, 5988; C. K. Chiang, C. R. Fincher, Y. W. Park, A. J. Heeger, H. Shirakawa, E. J. Louis, S. C. Gau, A. G. MacDiarmid, Phys Rev Lett 1977, 39, 1098.

[4] R. Noriega, J. Rivnay, K. Vandewal, F. P. V. Koch, N. Stingelin, P. Smith, M. F. Toney, A. Salleo, Nat Mater 2013, 12, 1038; X. Zhang, H. Bronstein, A. J. Kronemeijer, J. Smith, Y. Kim, R. J. Kline, L. J. Richter, T. D. Anthopoulos, H. Sirringhaus, K. Song, M. Heeney, W. Zhang, I. McCulloch, D. M. DeLongchamp, Nature Communications 2013, 4.

[5]   H. Sirringhaus, P. J. Brown, R. H. Friend, M. M. Nielsen, K. Bechgaard, B. M. W. Langeveld-Voss, A. J. H. Spiering, R. A. J. Janssen, E. W. Meijer, P. Herwig, D. M. de Leeuw, Nature 1999, 401, 685; J.-F. Chang, B. Sun, D. W. Breiby, M. M. Nielsen, T. I. Sölling, M. Giles, I. McCulloch, H. Sirringhaus, Chemistry of Materials 2004, 16, 4772; R. J. Kline, M. D. McGehee, E. N. Kadnikova, J. Liu, J. M. J. Fréchet, M. F. Toney, Macromolecules 2005, 38, 3312; R. Joseph Kline, M. D. McGehee, M. F. Toney, Nature Materials 2006, 5, 222; U. W. Gedde, *Polymer Physics*, Springer, 2008.

[6]   S. Patra, N. Munichandraiah, Journal of Applied Polymer Science 2007, 106, 1160; G. Wang, X. Tao, R. Wang, Composites Science and Technology 2008, 68, 2837; G. Latessa, F. Brunetti, A. Reale, G. Saggio, A. Di Carlo, Sensors and Actuators B: Chemical 2009, 139, 304; L. Zhu, Q. Dai, Z.-F. Hu, X.-Q. Zhang, Y.-S. Wang, Optics Letters 2011, 36, 1821.

[7]   G. H. Kim, L. Shao, K. Zhang, K. P. Pipe, Nat Mater 2013, 12, 719.

[8]   O. Bubnova, Z. U. Khan, H. Wang, S. Braun, D. R. Evans, M. Fabretto, P. Hojati-Talemi, D. Dagnelund, J.-B. Arlin, Y. H. Geerts, S. Desbief, D. W. Breiby, J. W. Andreasen, R. Lazzaroni, W. M. Chen, I. Zozoulenko, M. Fahlman, P. J. Murphy, M. Berggren, X. Crispin, Nat Mater 2013, 13, 190.

[9]   F. Jonas, J. T. Morrison, Synthetic Metals 1997, 85, 1397; L. Groenendaal, F. Jonas, D. Freitag, H. Pielartzik, J. R. Reynolds, Advanced Materials 2000, 12, 481.

[10]   S. G. Im, K. K. Gleason, Macromolecules 2007, 40, 6552; R. M. Howden, E. D. McVay, K. K. Gleason, Journal of Materials Chemistry A 2013, 1, 1334.

[11]   A. M. Coclite, R. M. Howden, D. C. Borrelli, C. D. Petruczok, R. Yang, J. L. Yagüe, A. Ugur, N. Chen, S. Lee, W. J. Jo, A. Liu, X. Wang, K. K. Gleason, Advanced Materials 2013, 25, 5392; S. G. Im, P. J. Yoo, P. T. Hammond, K. K. Gleason, Advanced Materials 2007, 19, 2863.

[12]   D. Joung, S. I. Khondaker, Physical Review B 2012, 86.

[13]   B. E. Warren, *X-Ray Diffraction*, Dover, 1990.

[14]   L. G. Kaake, P. F. Barbara, X. Y. Zhu, The Journal of Physical Chemistry Letters 2010, 1, 628.

[15]   A. J. Epstein, W. P. Lee, V. N. Prigodin, Synthetic Metals 2001, 117, 9; N. F. Mott, E. A. Davis, *Electronic Processes in Non-Crystalline Materials*, Oxford University Press, USA 2012.

[16]   P. Pipinys, A. Kiveris, Central European Journal of Physics 2012, 10, 271.

[17]   Y. H. Kim, C. Sachse, M. L. Machala, C. May, L. Müller-Meskamp, K. Leo, Advanced Functional Materials 2011, 21, 1076; M. Vosgueritchian, D. J. Lipomi, Z. Bao, Advanced Functional Materials 2012, 22, 421.
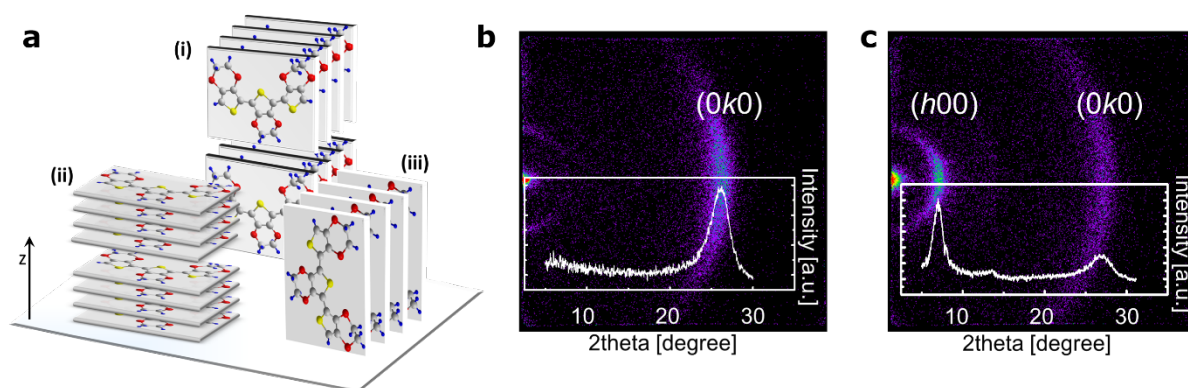
Figure 1. a) Three possible orientations for ordered PEDOT chains with respect to the substrate plane, two of which have their conjugated backbones parallel to the interface, (i) and (ii), while the orientation is perpendicular for (iii). The XRD maps (θ-2θ) for b) ungrafted and c) grafted oCVD PEDOT. Only ($0k0$) reflections appear for the ungrafted film, corresponding to the parallel orientation (ii). For the grafted film, both ($h00$) and ($0k0$) reflections are observed, indicating the presence of (i) and (ii) orientations.
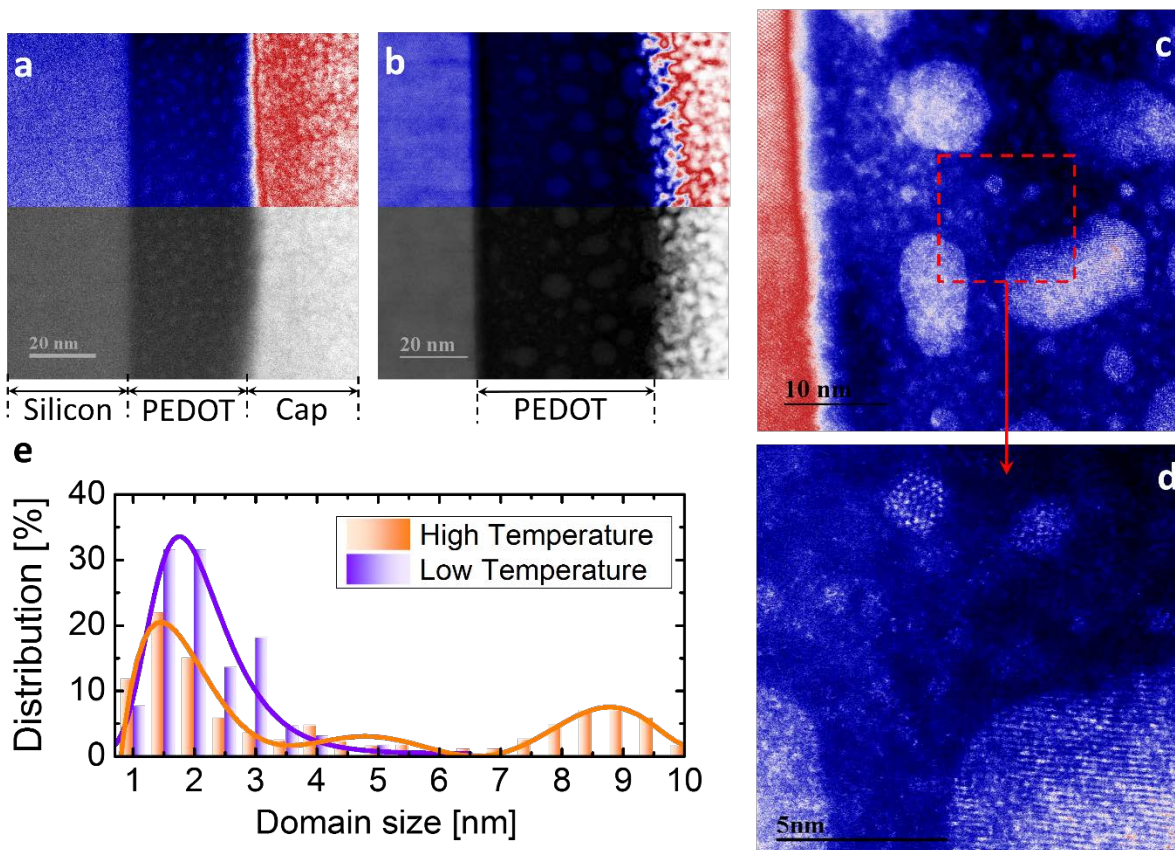
Figure 2. The High Angle Annular Dark Field (HAADF) Scanning Transmission Electron Microscopy (STEM) image of Cross sections of the interfaces of grafted PEDOT films grown at a) 100 °C and b) 200 °C. The top halves of both images are color-enhanced to clearly elucidate the crystalline domains surrounded by an amorphous matrix. High-resolution images for the film synthesized at 200 °C are shown in c) and enlarged in d), providing a direct evidence on the well-oriented large crystallites. e) Histogram of statistical domain size distribution obtained from images (a) and (b), showing the broader distribution and larger crystallite size for the film grown at high temperature (200 °C). STEM images indicate all three possible orientations for grafted samples as shown in Figure 1a (see SOM for detail).
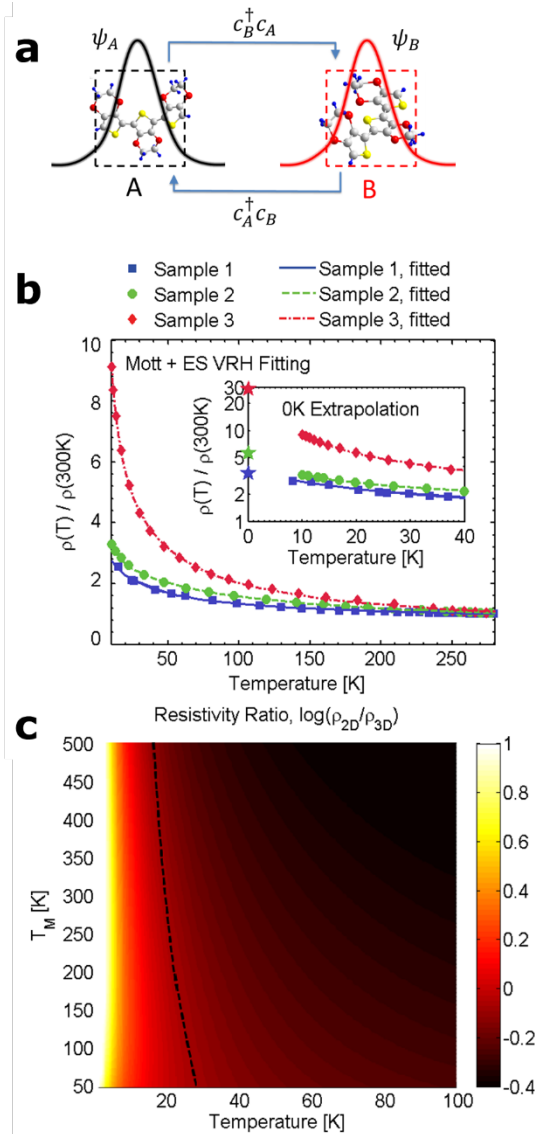
Figure 3. The measured conductivities and predicted values from the combined Mott + ES VRH model (Eq. 1). a) Microscopic representation of coarse-grain model for different domains is illustrated. Electron wave functions in crystalline domains A and B are denoted as ψ_A and ψ_B, respectively, which are also separated by an amorphous region. The conductivity originates from hopping of the electrons. The hopping from *B* to *A* is depicted as $c_A^+ c_B$. b) Low temperature resistivity measurements for Sample #1 is grown at 200 °C in where 2D conduction is dominated (52 nm), sample #2 is grown at 200 °C where the 3D conduction is dominated (124 nm), and sample #3 is grown at 100 °C where 3D conduction is dominated (145 nm). Inset figure

shows the normalized resistivity at low-temperature region with a highlight of 0 K extrapolation.

c) Extended model represented as logarithmic of the normalized resistivity ratio $\log(\rho_{2D}/\rho_{3D})$

between a 2D-like sample and a 3D-like sample via varying the parameter T_M and T. The black

dot trend line separates the region greater than 0 (2D has larger resistivity) and smaller than 0
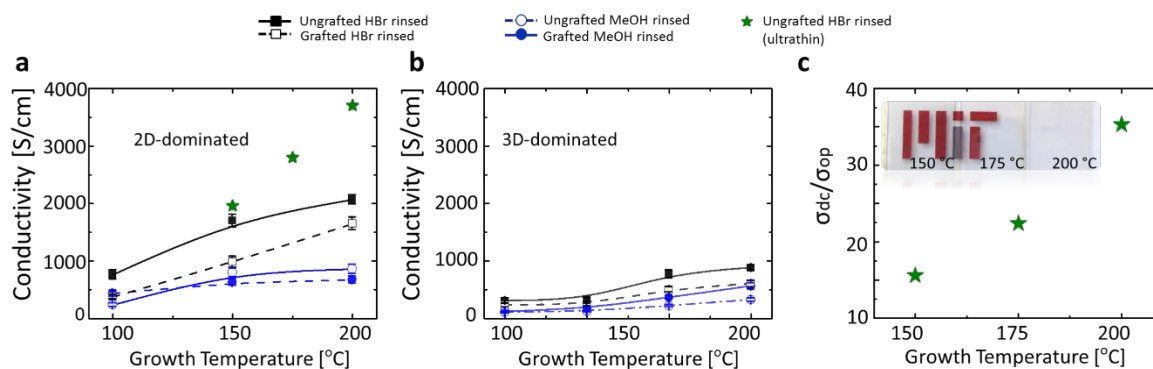
(2D has smaller resistivity).

Figure 4. The magnitude of room temperature conductivity for different sample sets comprises

3D-like where amorphous region is dominated and/or 2D-like where crystallite region is

dominated. a) Single step deposition of films < 80 nm thick (2D-dominated). The highest

conductivity (star symbols) is for films <10 nm thick. b) Single-step deposition of films >100 nm

thickness (3D conductivity). c) The dc conductivity to optical conductivity ratios (σ_{dc}/σ_{op}) of

ultra-thin highly conductive PEDOT films (<10nm). Inset shows the highly transparent PEDOT

films on glass slides.

Supporting Information

Title: Low-Dimensional Conduction Mechanisms in Highly-Conductive and Transparent Conjugated Polymers

Asli Ugur, Ferhat Katmis, Mingda Li, Lijun Wu, Yimei Zhu, Kripa K. Varanasi*, Karen K. Gleason*

Sample preparation

Both grafted and ungrafted oCVD PEDOT films were grown on Si(100) substrate having a

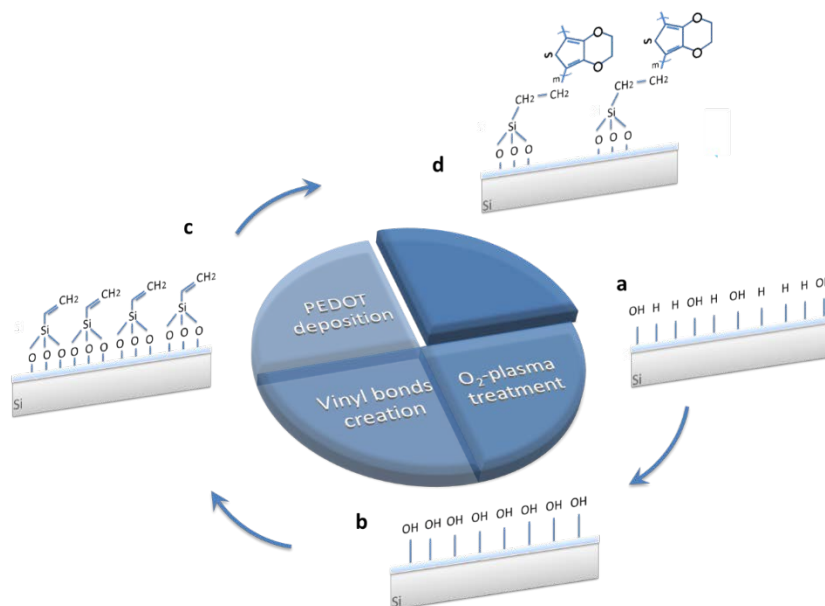native silicon oxide layer (schematic illustration is shown in **Figure S1**).

Figure S1. Schematic illustration for grafting PEDOT on Silicon substrate is shown. a) Surface of silicon substrate with native oxide layer. b) For grafting PEDOT on silicon substrate with native silicon oxide layer, the surface is treated with oxygen plasma to form hydroxyl groups. c) The sample is then exposed to trichlorovinylsilane (TCVS) to form a vinyl terminated surface. d) PEDOT is deposited as the last step where it can graft to the surface.

After deposition, the samples were rinsed with methanol (MeOH) for 5 minutes to remove

byproducts of the oxidation reaction and any excess reactants and from the film. Next, when

noted, an acid rinsing step for 30 minutes with 5 M diluted diatomic hydrobromic acid (HBr) is

performed on some samples to cause the dopant exchange from Cl- to Br- counterions to

enhance conductivity.[1]

Investigated samples

Different varieties of sample sets are prepared and investigated in this work. The samples for

XRD, STEM, and temperature dependent conductivity measurements

Samples for	Detail	Used in
XRD	Grafted, HBr rinsed, 180 nm, grown at 160 °C	Fig. 1a
	Ungrafted, HBr rinsed, 175 nm, grown at 160 °C	Fig. 1b
	Ungrafted, MeOH rinsed, 169 nm, grown at 160 °C	Fig. S2a
	Grafted, MeOH rinsed, 179 nm, grown at 160 °C	Fig. S2b
STEM	Grafted, HBr rinsed, 37 nm, grown at 100 °C	Fig. 2a
	Grafted, HBr rinsed, 52 nm, grown at 200 °C	Fig. 2b
Low T measurement	Sample #1 Ungrafted, HBr rinsed, 52 nm, grown at 200 °C	Fig. 3b
	Sample #2 Ungrafted, HBr rinsed, 124 nm, grown at 200 °C	
	Sample #3 Ungrafted, HBr rinsed, 145 nm, grown at 100 °C	

X-ray diffraction (XRD) on samples

These XRD measurements utilized a high power multipurpose diffractometer configured with a

CuK$_\alpha$ radiation (λ = 0.15418 nm).

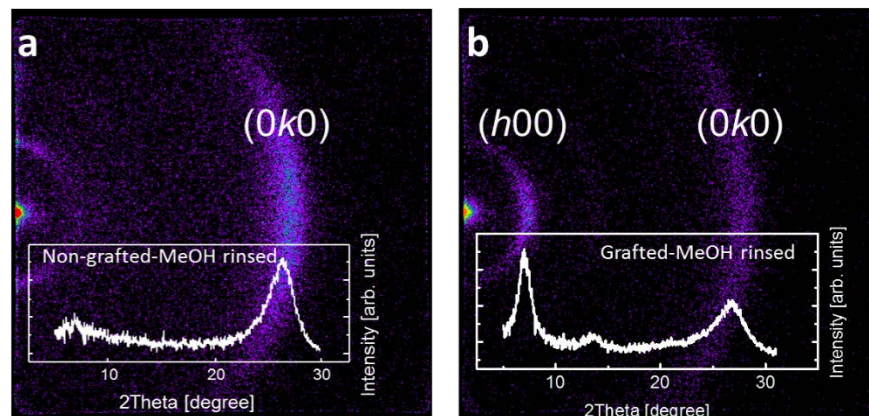**Figure S2.** a) (θ-2θ) scan of oCVD PEDOT on Si along the growth direction for ungrafted MeOH rinsed, where (0k0)-type is dominant and b) (θ-2θ) scan of grafted MeOH rinsed, where both (h00)-type and (0k0)-type reflection families are observable, however (0k0) is highly suppressed.

2-dimensional mappings were performed via "Bruker D8 Discover with GADDS". The instrument uses a Vantec2000 2D detector to collect a large amount of data simultaneously, this allows for very fast phase identification, as well as; quickly identify preferred orientation(s). The diffractometer has an open Eularian cradle for tilt (psi) and rotation (phi) of the sample and motorized xyz stage for positioning of the sample. We used 1" x 1" samples for XRD scans. After careful alignment of the sample, the sample surface is illuminated with 40 kV and 40 mA beam at a fixed omega angle. To get a high-intensity we used monocapillary (fiber-optic) collimator (0.3 mm diameter size). The detector is placed 18.61 cm away from the sample axis. Rather than collecting a continuous 1D scan like a conventional diffractometer, we use 2D detector to take a snapshot at the same angle for long exposure time and the line cut is presented in the same frame. Our measurement geometry is conventional horizontal theta-2theta. With this measurement geometry and experimental XRD data we can only talk about domain sizes, and preferred orientations within the layers.

Crystalline size determination: The d-spacings obtained from profile fitting of XRD diffraction curves are 1.36 nm for (h00)-type diffraction and 0.34 nm for (0k0)-type. It has been previously shown that PEDOT has orthorhombic crystal structure.[2] Additional XRD for MeOH rinsed samples are shown for grafted and ungrafted layers in **Figure S2**.

Sample preparation for electron diffraction

The cross sectional thin film specimens were prepared using Helios Nanolab 600 Dua-Beam Focused Ion Beam Milling System operated at low voltages (5 kV and 1 kV) to minimize the damage to polymer and reduce the Ga ions contamination.

The morphology and structural properties of the layers were separately investigated by scanning transmission electron microscopy (STEM) and high-angle annular dark field (HAADF) STEM is employed here using the same microscope, which is equipped with a scanning unit and a HAADF detector. The STEM-HAADF images were taken in scanning mode in our double aberration corrected transmission electron microscope with high angle annular dark field (HAADF) detector with JOEL ARM 200CF S/TEM, at Brookhaven National Lab. The collection angle is from 67 mrad to 275 mrad. The advantage with STEM-HAADF image is that its contrast is proportional to Z (atomic number), and give sharp image contrast for thick samples comparing to TEM BF and DF images.

We used low energetically electron, such as 80 keV electron beam, to minimize the beam damage for all samples. The probe current is 4.6 pA. The total exposure time for the image is

only 8 seconds. In this very careful conditions, we observed crystalline domains and we do not see any beam damage while imaging. To get better image quality in high-crystalline samples, 200 keV electron with an 18.5 pA probe current is used.

The contrast (or image intensity) of STEM-HAADF is basically proportional to the Z (Z: atomic number) square. The bright domains we observed indicate that their Z is heavier. Thus the dark contrast in STEM-HAADF image corresponds to low Z, or low density in the area, especially for amorphous materials. Beyond that, any kind of strain may further reduce the STEM-HAADF intensity. The crystal domains in grafted sample grown at low temperature (SLow) is smaller than the grafted sample grown at high temperature (SHigh). Moreover, we clearly see the lattice fringes in grafted SHigh crystal domains, while not quite in grafted SLow samples, indicating the domains in grafted SHigh is better ordered than those in SLow due to efficient doping of SHigh samples.

Theoretical Modelling

Note that the nanocrystalline structure is probably not thermodynamically stable but rather a kinetically trapped configuration. This is why annealing causes a further increase in crystallinity. In case of perfect ordering of polymer chains the ordering parameter (η) approaches to 1 which means all the chains are aligned along a certain crystallographic direction (**Figure S3a**). Any chain distortion or deformation drift apart from 1 and approaches to 0 for fully disordered case (amorphous, **Figure S3b**). For nanocrystalline materials, both crystalline and amorphous region co-exist. The transition between two crystallite region likely happens via gradual change of η.

Illustration for possible coalescence of two domains, e.g. *A* and *B*, in the presence of amorphous region, where the ordering parameter or coefficient is $0<\eta<1$, is shown in **Figure S3c**.
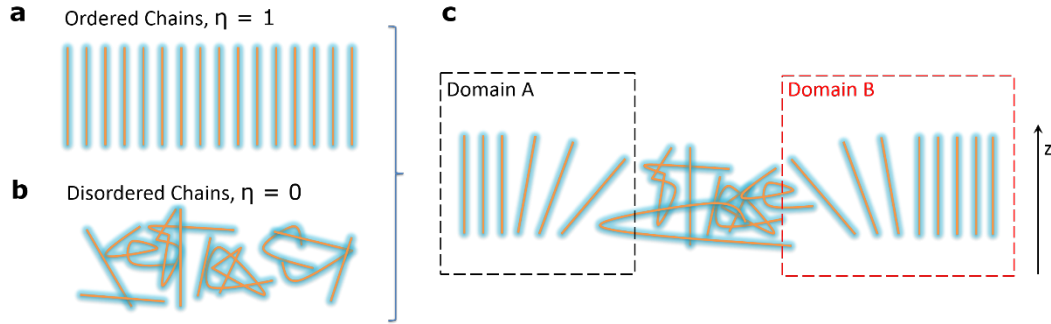

Figure S3. a) ordering parameter, $\eta=1$, all the chains are aligned along one particular crystallographic direction. For completely disordered (amorphous) chains in b), $\eta=0$, are shown. c) Schematic of the coexistence of nanocrystals and amorphous regions. A gradual change of η can result in the coalescence of two domains, e.g. *A* and *B*.

Mott's VRH $\qquad\qquad\qquad\qquad \beta\exp\left[\left(\frac{T_M}{T}\right)^{\frac{1}{d+1}}\right]$ $\qquad\qquad$ (S1)

Efros-Shklovskii VRH $\qquad\qquad \beta\exp\left[\left(\frac{T_{ES}}{T}\right)^{\frac{1}{2}}\right]$ $\qquad\qquad$ (S2)

Simplest form of Mott E-S + VRH $\qquad \beta\left(\exp\left[-\left(T_M/T\right)^{\frac{1}{1+d}}\right]+\exp\left[-\left(T_{ES}/T\right)^{\frac{1}{2}}\right]\right)^{-1}$ $\qquad$ (S3)

where β, T_M, and d defined as dimensionless amplitude for Mott VRH model, Mott transition temperature, and effective dimension, respectively. The contribution of conductivity from Mott's VRH can be written as $\ln\rho(T)\propto\left(T_M/T\right)^{1/(d+1)}$, and $T_M\propto a^3$ is the Mott transition temperature with a defined as the inverse localization length.[3] We normalize the resistivity with the respective value of resistivity at 300 K, and fit it using the Mott's VRH model (**Figure S4**), which seems

not perfectly match the experimental data points for sample #3. The fitting parameters are

summarized in Tab. S1 for comparison to other samples.

Fitting	B	T_M	d	Residual
Sample #1	0.65868	50.912	2	0.0011112
Sample #2	0.24142	1287	3	0.01058
Sample #3	0.10965	7547.6	3	0.049481

Tab. S1 The fitting results using Mott's VRH theory, equation S1. β, T_M, and d defined as dimensionless amplitude for Mott VRH model, Mott transition temperature, and dimension, respectively.
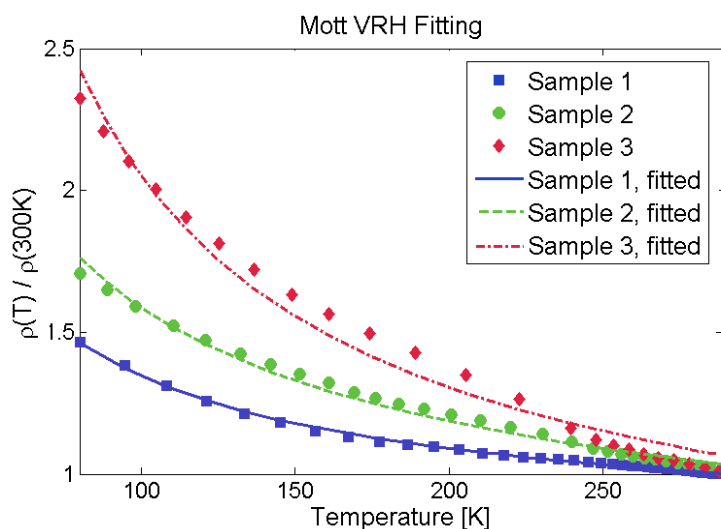

Figure S4. The results of fitting using Mott's VRH theory.

From the fitted results, we see that the fitted effective dimension of sample 1 is $d = 2$, while

sample 2 and 3 have effective dimension $d = 3$. This indicates that sample 1 has the thinnest

thickness, which is indeed the situation.

Fitting	β_1	T_M	d	β_2	Residual
Sample #1	0.81498	50.39	1	0.69948	0.0011579

7

Sample #2	1.9481	172.36	3	6.7402	0.00058892
Sample #3	3.7348	1624.5	3	116.2	0.0034478

Tab. S2 The fitting results using Mott's and E-S VRH theory. β, T_M, and d defined as dimensionless amplitude for Mott VRH model, Mott transition temperature, and dimension, respectively.

The conductivities in **Figure 4** are the inverse product of the sheet resistance, measured using a 4-point probe, and the polymer film thickness. In these calculations, the important parameter thickness was accurately measured by low-angle XRR, a non-contact and non-destructive method with ±0.09 nm accuracy,[4] as opposed to the more commonly used contact-mode profilometry technique. Since the PEDOT polymer is soft, plastic deformation of the polymer surface by the stylus of the profilometer can result in measurement errors.[5, 6] While it might be anticipated that the contact would cause indentation into the film and thus systematically lower values,[6] the profilometer obtained values in this work were found to be consistently higher than the XRR data, suggesting that extra material is being measured, as would be the case if polymer was being transferred to the stylus.
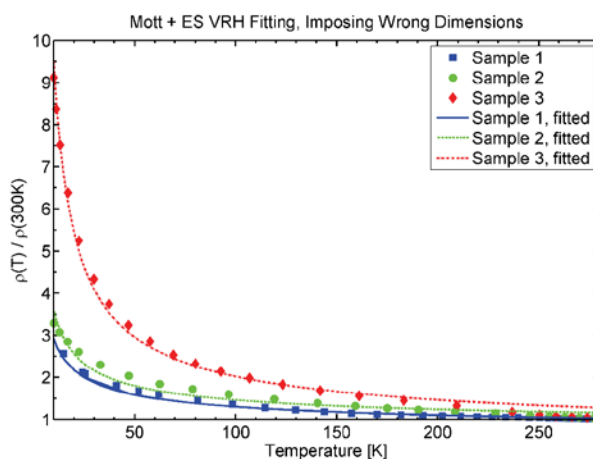

Figure S5. The fitting results for mean square error using Mott's and E-S VRH theory by imposing wrong and correct dimensions on all samples. Simply by forcing sample #1 to be 3D, sample #2 to be 2D, and sample #3 to be 2D against the correct dimensions with low residual.

Mean square error	Sample #1	Sample #2	Sample #3

correct dimensions	0.001158	0.00058889	0.0034478
forced fitting dimensions	0.32239	0.81119	1.6401

Tab. S3 The fitting results for mean square error using Mott's and E-S VRH theory by imposing wrong and correct dimensions.
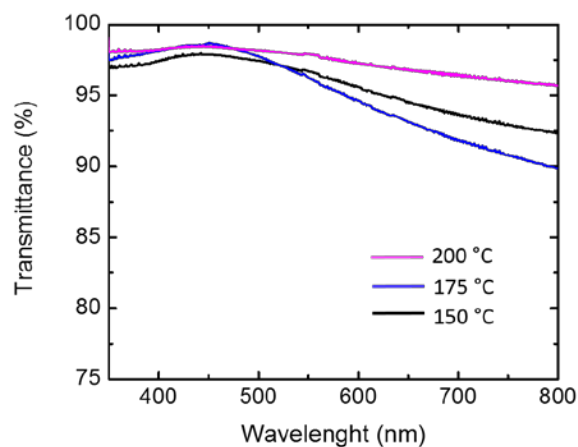
Transmittance

Figure S6. Optical transmission spectra in the visible regime wavelengths of HBr rinsed samples.

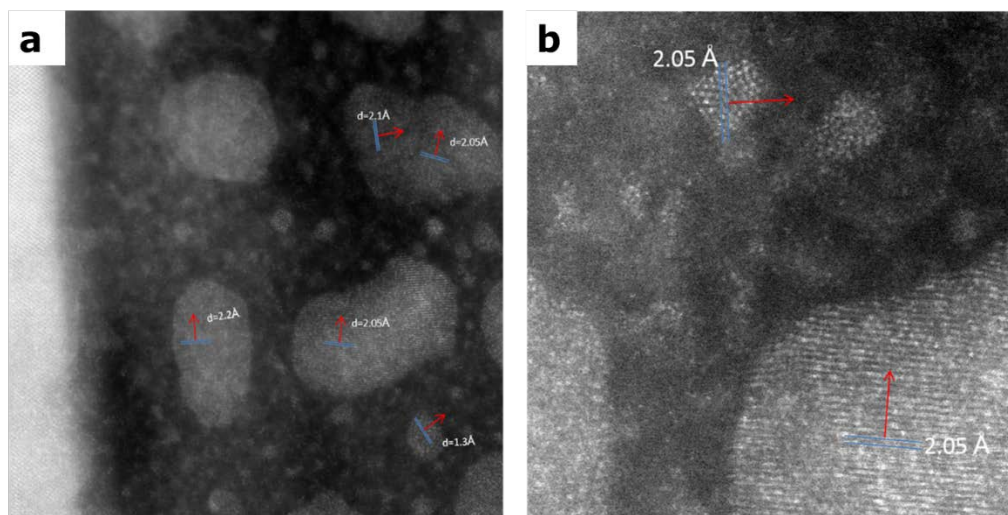**Additional supportive experimental data**

Figure S7. a) STEM image and b) zoomed STEM image for grafted sample. Measured d-spacing are shown with the blue lines and plane normal is shown with red arrows. The d-spacing of the

fringes is close to (004) and (006) of PEDOT within 5 % error (comes from Br-doping effect), indicating the structure of the smaller nano size domains, which have reduced periodicity. Due to nano size dimensions of those (00*l*)-type domains, we cannot observe them with conventional XRD and can only be measured by TEM.

[1]   R. M. Howden, E. D. McVay, K. K. Gleason, Journal of Materials Chemistry A 2013, 1,

        1334.

[2]   K. E. Aasmundtveit, E. J. Samuelsen, L. A. A. Pettersson, O. Inganäs, T. Johansson, R.

        Feidenhans'l, Synthetic Metals 1999, 101, 561.

[3]   P. Pipinys, A. Kiveris, Central European Journal of Physics 2012, 10, 271; A. J. Epstein,

        W. P. Lee, V. N. Prigodin, Synthetic Metals 2001, 117, 9.

[4]   A. Ulyanenkov, R. Matsuo, K. Omote, K. Inaba, J. Harada, M. Ishino, M. Nishii, O. Yoda,

        Journal of Applied Physics 2000, 87, 7255; A. Gibaud, A. Hazra, Current Science 2000,

        78; J. Tiilikainen, J. M. Tilli, V. Bosund, M. Mattila, T. Hakkarainen, J. Sormunen, H.

        Lipsanen, Journal of Physics D: Applied Physics 2007, 40, 7497.

[5]   M. V. Fabretto, D. R. Evans, M. Mueller, K. Zuber, P. Hojati-Talemi, R. D. Short, G. G.

        Wallace, P. J. Murphy, Chemistry of Materials 2012, 24, 3998.

[6]   M. Fabretto, K. Zuber, C. Jariego-Moncunill, P. Murphy, Macromolecular Chemistry and

        Physics 2011, 212, 2173.